released, a new solid phase having the *Pc* space group forms at ambient conditions [63]. Both the starting and the ending solid phases in this process have comparable stability, pointing toward the conservation of the structural motifs upon decompression. This example illustrates that different polymorphs formed after pressurization change only their intermolecular packing, and no degradation of the cage molecules occurs because of their stable diamond-like structure, which is a significant advantage over other types of organic materials. What is more, the molecular geometry of the individual cages also affects the compressibility of the corresponding crystal, making diamondoids of different shapes a rich toolbox of nano-sized building blocks for organic, high-pressure material design.

1.5 Spectroscopy of Diamondoids

The uniqueness of unfunctionalized diamondoids when compared to other hydrocarbons becomes especially apparent when noting their spectroscopic and photophysical properties [61]. Bulk diamond is a good electrical insulator with a large band gap. Luckily, with increasing diamondoid size, the HOMO–LUMO gap decreases and shows a tendency to converge close to the fundamental gap of bulk diamond [64]. For example, larger nanodiamonds with sizes up to 2 nm have computed band gap values of 6.7 eV as compared to 5.5 eV for bulk diamond [65]. Structurally well-defined nanodiamonds display strong quantum confinement effects at particle sizes ranging from 0.5 to at least 2 nm, but it is the size and not the shape of the particles that affect the band gap values. This was demonstrated by the comparison of octahedral vs. tetrahedral nanodiamonds that in the end showed the same trends in band gap narrowing. Since there appears to exist a limit to gap narrowing for nanodiamonds, a proposed method for further reduction of the gap is the introduction of external or internal doping substituents (C—H bond substitution and replacement of cage CH/CH_2 groups, respectively). As will be demonstrated in Chapter 12, doping is a very successful strategy for semiconductor applications of diamondoids. Note that such size-property relationships hold true not only for diamondoids but for parent diamond nanoparticles as well: particle sizes must be around 2 nm to start observing an increase in the optical gap (vide infra) [66]. In other words, reducing the size of bulk diamond to the nanoscale has a pronounced effect on the optical gap of the resulting nanoparticle, with a decrease in the optical gap by increasing nanoparticle size being more rapid for diamond than for, e.g., Si or Ge, where quantum confinement effects persist up to 6–7 nm.

Another computational study on diamondoids found that quantum confinement effects essentially disappear in diamondoid structures larger than 1 nm [67]. However, the applied Monte Carlo computations predict a small exciton binding energy and a negative electron affinity (NEA) for nanodiamonds of that size, which is a consequence of significant LUMO delocalization (Figure 1.13). Note here that the HOMO is predominately localized on the C—C bonds inside the nanoparticle, while the delocalized LUMO has a considerable probability outside of the surface boundaries and is mostly composed of the C—H bonds. With increasing

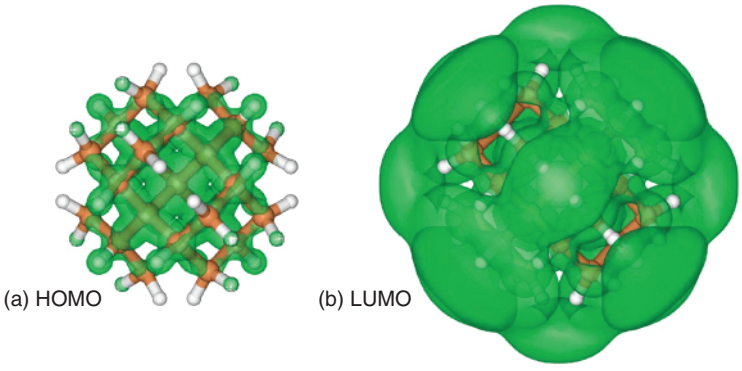

Figure 1.13 Isosurface plots of the square of the (a) HOMO and (b) LUMO of hydrogen-terminated spherical diamond-like nanoparticle $C_{29}H_{36}$. The green isosurfaces include 50% of the charge in each orbital. Source: Reproduced from Ref. [67] with permission from the American Physical Society, 2005.

nanoparticle size, the HOMO ultimately converges to the valence-band maximum of bulk diamond, while the LUMO remains near the surface boundary and does not become a conduction band minimum. Such an almost defect-like nature of the LUMO is the reason why the optical gaps of large diamondoids lie below the gap value of bulk diamond.

As the HOMOs predominately describe the C—C bonding, the vibrational motion of the carbon nuclei has a significant effect on the orbital energies, while the higher-lying orbitals are often Rydberg states that are more sensitive to the vibrational motion of the hydrogen atoms. It follows that in order to reliably compute the optical properties of diamondoids, quantum nuclear dynamics are needed to ensure accurate prediction of their photophysics [68]. Despite such theoretical requirements, recent time-dependent density functional theory (TD-DFT) approaches for vibrationally resolved photoelectron spectra simulations succeeded in coming very close to fully reproducing the experimentally observed vibrational fine structure [69]. What still remains to be tackled in that particular computational approach are errors in computed spectral redshifts upon increasing particle size due to the lack of many-body corrections, a trait that is inherent to the method, as well as the absence of satellites in the high-energy region of the spectra due to electron-nuclear coupling. Further computational studies confirmed that the high diamondoid symmetries lead to forbidden transitions [70]. However, it was also noted that using HOMO–LUMO gaps for the approximation of diamondoid optical gaps was somewhat of an oversimplification, especially since their absorption and emission spectra are vibronically highly structured and often accompanied by broadened and shifted optical bands.

When diamondoids approach the 1 nm range, their crystal morphology itself begins to affect their structural integrity [71]. Theoretical models predicted that while the initial cubic morphology provides relaxation structures comparable to bulk diamond itself, octahedral and cuboctahedral starting materials gradually transform from a pure sp^3 to a mixed sp^3 and sp^2 bonding network, essentially

converting the particle into partially unsaturated layered morphologies. This finding implies that spontaneous phase transitions of nanodiamond clusters starting from the outer carbon atom shells need to be taken into account when designing functional nanodevices. However, hydrogen-terminated diamondoids do not suffer from such layer transformation effects. Dehydrogenated octahedral and cuboctahedral nanodiamond particles up to 1 nm in diameter are therefore structurally unreliable and unstable morphologies that readily undergo partial graphitization and exfoliation of their (111) surfaces, which consequently opens up an important niche for applications. Density functional theory computations up to decamantane confirm this reasoning since hydrogen-terminated diamondoids indeed retain atomic arrangements and electronic structures similar to those of bulk diamond [64].

The computed equilibrium C—C bond lengths and bond angles for diamondoids are comparable to those of bulk diamond, providing them with diamond-like properties, especially as the size of the diamondoids increases. Quantum confinement effects were studied using X-ray absorption spectroscopy, and the resulting diamondoid gas phase spectra (Figure 1.14) show that blueshifts in the band edges do not occur with decreasing particle size, as would be expected for typical group IV semiconductors [72]. In other words, diamondoid clusters display some differences from bulk diamond, which can be advantageous for some applications.

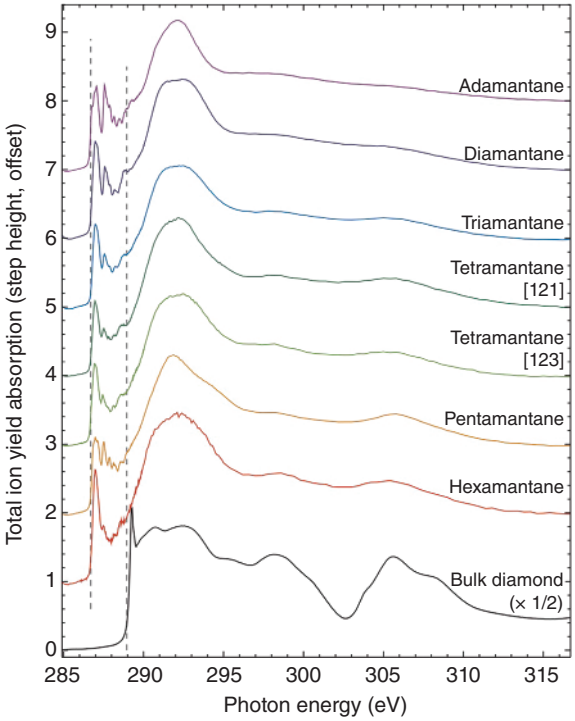

Figure 1.14 Carbon *K*-edge absorptions of selected diamondoids and bulk diamond. Source: Reproduced from Ref. [72] with permission from the American Physical Society, 2005.

While the information on HOMO–LUMO gaps is fundamentally important, the optical gaps (based on symmetry-allowed transitions) provide more relevant information on the properties of diamondoids. The optical gaps of diamondoids measured in the gas phase [73] are in agreement with the experimental and computed trends in changes of the HOMO–LUMO gaps but display strong shape dependence (Figure 1.15) within different topological families (3D, 2D, and 1D denote tetrahedral, prism, and rod-shaped diamondoids, respectively). This is due to the forbidden HOMO → LUMO transitions for some highly symmetric structures. The optical gaps primarily originate from the single-particle transition from HOMO to LUMO or to LUMO+1 and LUMO+2 depending on the selection rule. For instance, **TET** with C_{2h} symmetry (**121TET**) has the first dipole active transition between HOMO and LUMO+2, while HOMO → LUMO transitions are allowed for C_{3v} and C_2 **TET**s. Such symmetry dependence of optical gaps and excitation energy agreed fully with the experiment (Table 1.3).

While the optical gaps of $C_{26}H_{32}$ **1213PENT** (5.75 eV) and bulk diamond display remarkable similarities, the absolute value of 5.5 eV is still unreachable with diamondoids of this size. This agrees well with computations on larger diamondoids that also predict a rapid decrease of the absorption gap (Figure 1.16, left), which becomes similar to the computation for bulk diamond only for particles of about 1 nm in diameter ($C_{87}H_{78}$) [75].

More detailed TD-DFT computations on small diamondoids with the PBE0 method [74b] reveal that the first 3s-like Rydberg excitation is common for all diamondoids (Figure 1.16, right) except for C_{2h}-symmetric **121TET** and **12312HEX,** where such excitations are dipole-forbidden and, therefore, 3*p*-like Rydberg transitions occur instead. For tetrahedral **AD** and **1(2,3)4PENT** both $t_2 \rightarrow a_1(3s)$ and

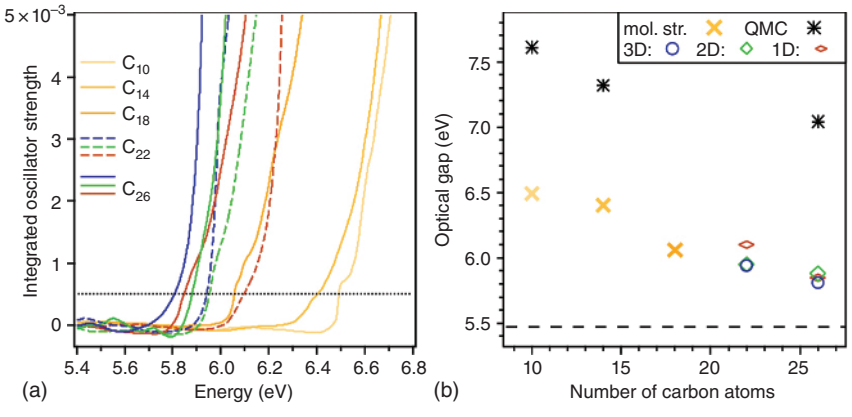

Figure 1.15 (a) Integrated oscillator strength measured for diamondoids **AD** (C_{10}), **DIA** (C_{14}), **TRIA** (C_{18}), as well as for isomeric tetramantanes (C_{22}) and pentamantanes (C_{26}). The threshold defining the optical gap is marked by a dotted line. (b) Experimental optical gaps as a function of size compared to optical gaps derived by quantum Monte Carlo (QMC) calculations. The dashed line marks the energy gap of bulk diamond, and 3D, 2D, and 1D denote tetrahedral, prism, and rod-shaped diamondoids, respectively. Source: Reproduced from Ref. [73] with permission from the American Physical Society, 2009.

Table 1.3 Ground state symmetries, TD-PBE0/aug-cc-pVTZ computed and experimental optical gaps (E_{gap}), and excitation energies of selected diamondoids based on photoluminescence measurements (Source: From [73, 74]).

Diamondoid	Symmetry	Formula	E_{gap} (eV) Comp.	E_{gap} (eV) Exp.	Excitation energy (eV) Exp.
AD	T_d	$C_{10}H_{16}$	6.66	6.49	6.49
DIA	D_{3d}	$C_{14}H_{20}$	6.75	6.40	6.60
TRIA	C_{2v}	$C_{18}H_{24}$	6.12	6.06	6.78
121TET	C_{2h}	$C_{22}H_{28}$	6.25	**6.10**	**6.88**
1(2)3TET	C_{3v}	$C_{22}H_{28}$	6.04	**5.94**	**5.99**
123TET	C_2	$C_{22}H_{28}$	6.01	**5.95**	**5.98**
1(2,3)4PENT	T_d	$C_{26}H_{32}$	5.99	5.81	5.93
12(1)3PENT	C_1	$C_{26}H_{32}$	–	5.83	6.20
1212PENT	C_{2v}	$C_{26}H_{32}$	5.86	5.85	–
1213PENT	C_1	$C_{26}H_{32}$	–	5.75	6.31

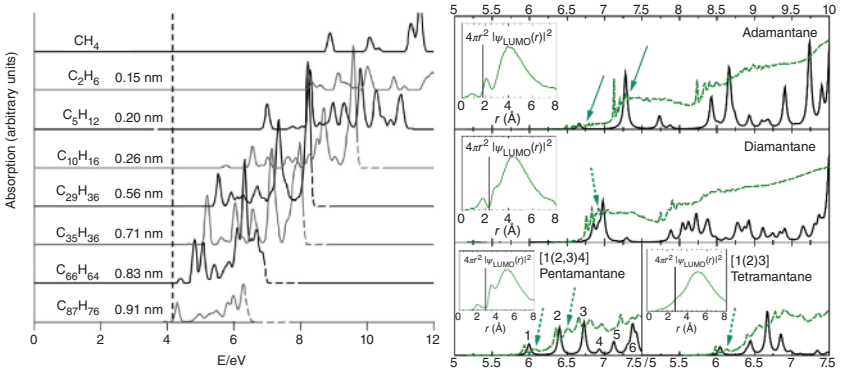

Figure 1.16 *Left*: TD-DFT-computed absorption spectra of diamondoids up to 1 nm in diameter. The vertical dashed line corresponds to the computed absorption gap of bulk diamond. (Source: Reproduced from Ref. [75] with permission from Elsevier, 2005.) *Right*: Computed and experimental absorption spectrum for selected diamondoids. The green (dashed) line shows the experimental spectrum, while the black (continuous) line is the computed spectrum. Inset: radial distribution of 3*s*-like Rydberg state, where vertical line represents the radius of diamondoid. Source: Reproduced from Ref. [74b] with permission from the American Physical Society, 2009.

$t_2 \rightarrow t_2(3p)$ transitions are allowed, but the latter has a higher density of states that leads to a larger absorption for the 3*p*-Rydberg excitation [75].

Diamondoids display intrinsic photoluminescence in the ultraviolet spectral region [76]. For example, **AD** exhibits a quite broad UV luminescence band when photoexcited in the gas phase above its principal optical gap of 6.49 eV (Table 1.3)

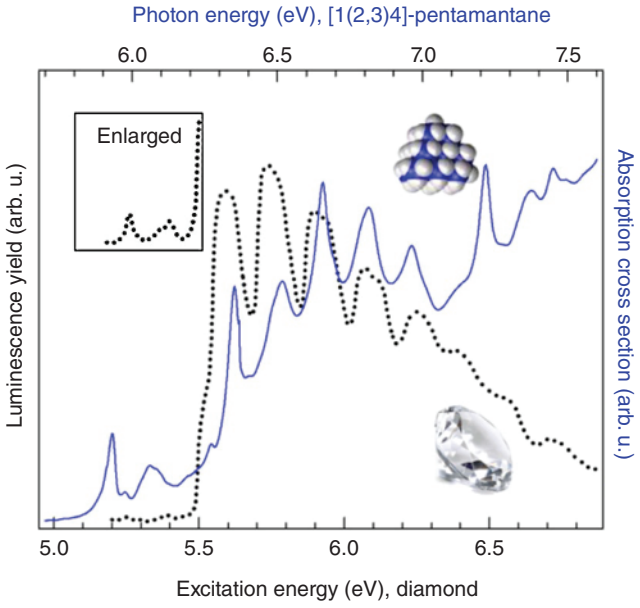

Figure 1.17 Comparison of the optical absorption of **1(2,3)4PENT** (blue line) with the absorption of high-purity type IIa diamond (dotted line). The spectral inset shows the enlarged onset of the bulk diamond spectra. Source: Reproduced from Ref. [73] with permission from the American Physical Society, 2009.

[73]. The optical gap characteristic for diamondoids thus lies in the UV spectral region [77], and the luminescence behavior is attributed to a transition from the delocalized first excited state into different vibrational modes of the electronic ground state [74a]. The majority of such transitions originate from vibrational modes associated with CH wagging and CH_2 twisting of the diamondoid surface atoms (vide infra) [78]. Difficulties in computationally predicting exact lineshapes of diamondoid photoemission spectra arise from electron-vibration coupling that cannot be corrected by applying simple vibration-broadening corrections to the corresponding electronic states [79]. Importantly, the overall optical absorption of diamondoids noticeably changes as a function of their size and shape, and in the case of **1(2,3)4PENT,** the spectrum begins to resemble that of bulk diamond (Figure 1.17). In other words, optical properties change as larger diamondoids are used, demonstrating that diamondoids could form valuable semiconductor nanocrystals for application in light-emitting devices in the deep UV spectral region.

1.6 Ionization Potentials

Since spectral data suggest that diamondoids are also present in space [80], matrix isolation techniques were used to mimic astrophysical conditions. After the deposition of diamondoids in a neon matrix, they were irradiated with high-energy photons, and UV absorption spectra were recorded. This revealed the presence of

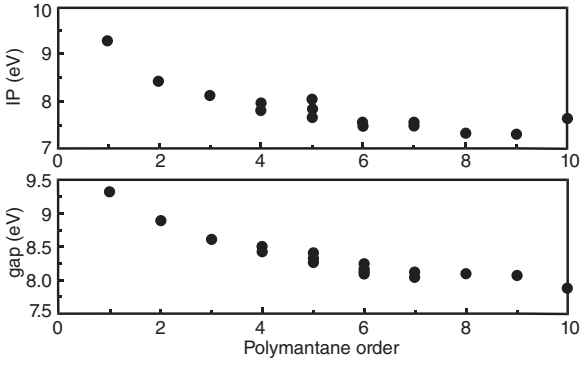

Figure 1.18 Ionization potentials (top) and HOMO–LUMO gaps (bottom) of diamondoids vs. polymantane order. Source: Reproduced from Ref. [83a] with permission from the American Physical Society 2005.

AD and **DIA** cations [81]. However, larger diamondoids starting from **TRIA** could already be ionized by far UV irradiation, and the absorbed energy apparently was distributed through a vibrational mechanism, thereby preventing hydrogen abstraction. An especially fascinating finding was that the spectra obtained from these experiments exhibit noticeable similarities to the spectra obtained from nanodiamonds extracted from the Allende meteorite [82]. We therefore next focus on the diamondoid ionization potentials (IPs) because they are such a fundamentally important property of materials in general. The IPs and HOMO–LUMO gaps decrease with increasing diamondoid order (Figure 1.18) and are well-reproduced by computations [21], but adiabatic IP values are systematically underestimated [67, 83]. Quantitative studies [83b] using total-ion-yield spectroscopy utilizing the commonly used linearization procedure revealed a trend of decreasing adiabatic IP values as a function of diamondoid size, with **AD** having IP = 9.23 eV and going down to 8.07 eV for **1(2,3)4PENT**. In the case of **AD** and cyclohexane as a reference, the agreement with the NIST [84] data is very good. Diamondoids form highly delocalized ionized states whose structures will be discussed in detail in Chapter 4; studying them was attempted by many but is still experimentally challenging.

1.7 Electron Affinities

Alkanes display negative electron affinities (EAs) [85], and the anions derived from saturated hydrocarbons are metastable, where the methane radical anion is the prototype [86]. The experimental observation of the adamantane radical anion ($\mathbf{AD}^{-\cdot}$) was attempted in 1963 [87] but was unsuccessful [88]. The DFT geometry optimization and frequency analysis of the anionic $^2A_1$ state of **AD** [89] display a minimum at T_d symmetry with altering C—C distances in the cage and slightly elongated CH bonds. As only small geometric changes occur upon reduction, the vertical and adiabatic EAs of **AD** are close and range from −1.0 to −0.5 eV [89, 90]. The ultraviolet photoelectron spectroscopy (UPS) spectra of the thick (27 Å) **AD** layer on the Cu(111) surface [91] estimate the EA of solid **AD** as −0.3 eV. The diffusion Monte Carlo simulations [67] predict a negative EA of −0.13 and − 0.26 eV for **AD** and **1(2,3)4PENT**, respectively. The plane-wave DFT computations also

show a negative EA of −0.3 eV for **121TET** [92]. The ability to form highly ordered surface self-assembled monolayers in combination with negative EAs determines the potential of diamondoids for the construction of cold electron emitters and is discussed in detail in Chapter 5.

1.8 Vibrational Spectroscopy

As could be expected from their hydrocarbon nature, infrared spectroscopy of diamondoids produces relatively straightforward absorptions that can be considered a spectral fingerprint of this class of compounds. There exist several general groups of signals corresponding to their vibrational modes: C—H stretching modes around 2900 cm^{-1}, CH_2 scissoring modes (commonly as doublets) around 1450 cm^{-1}, C—H bending and CH_2 rocking, wagging, and twisting modes between 1000 and 1400 cm^{-1}, C—C stretching around 1000 cm^{-1}, and skeletal deformation modes below 1000 cm^{-1} [93]. The existence of such characteristic spectral signals can be used as a means of detection for the presence of diamondoids, for example, in deep space, where nonspectral characterization methods are not applicable [80c]. The computational approaches for evaluating vibrational spectra of diamondoids were found to reproduce the experimental spectral signals well, meaning they can be effectively used for predicting spectra of even higher diamondoids, as was demonstrated in the case of cyclohexamantane [93, 94]. The most characteristic IR bands of higher diamondoids (C—H stretching modes around 2900 cm^{-1} and doublet around 1450 cm^{-1} of CH_2 scissoring modes) are computationally reproduced very well and are almost independent of the basis set [93]. The same is true even for the fingerprint region (1000–1400 cm^{-1}). The experimental Raman spectra have been nearly completely assigned based on comparison with DFT-computed vibrational frequencies and Raman intensities. Each diamondoid produced a unique Raman spectrum (Figure 1.19), which allows for differentiation between the structures. A very good agreement is observed between the experimental [50] and computed [96] vibrational spectra of **12312HEX**.

From the above, it seemed that the experimental absorptions in the CH-stretching region are not very characteristic for the assignment of a diamondoid structure. However, the high-resolution inelastic STM-based IR spectroscopy (IRSTM) of submonolayers of **121TET** and **123TET** on Au(111) enables the distinguishing between the structures clearly (Figure 1.20).

Computations on large (up to 1.92 nm) H-terminated nanodiamond particles show that the major IR peaks in the region of 900–1300 cm^{-1} shift toward high wavenumbers as size increases, while the C—H vibrations in the range show the opposite trend [98].

UV resonance Raman spectroscopy has been used to characterize **DIA** *syn*- and *anti*-dimers that contain a central C—C double bond [99], and it was found that their observed Raman resonance energies were significantly lower than the HOMO–LUMO gaps of the corresponding unmodified diamondoids. Thus, compound screening when modifying the optical gap in diamondoids by functional

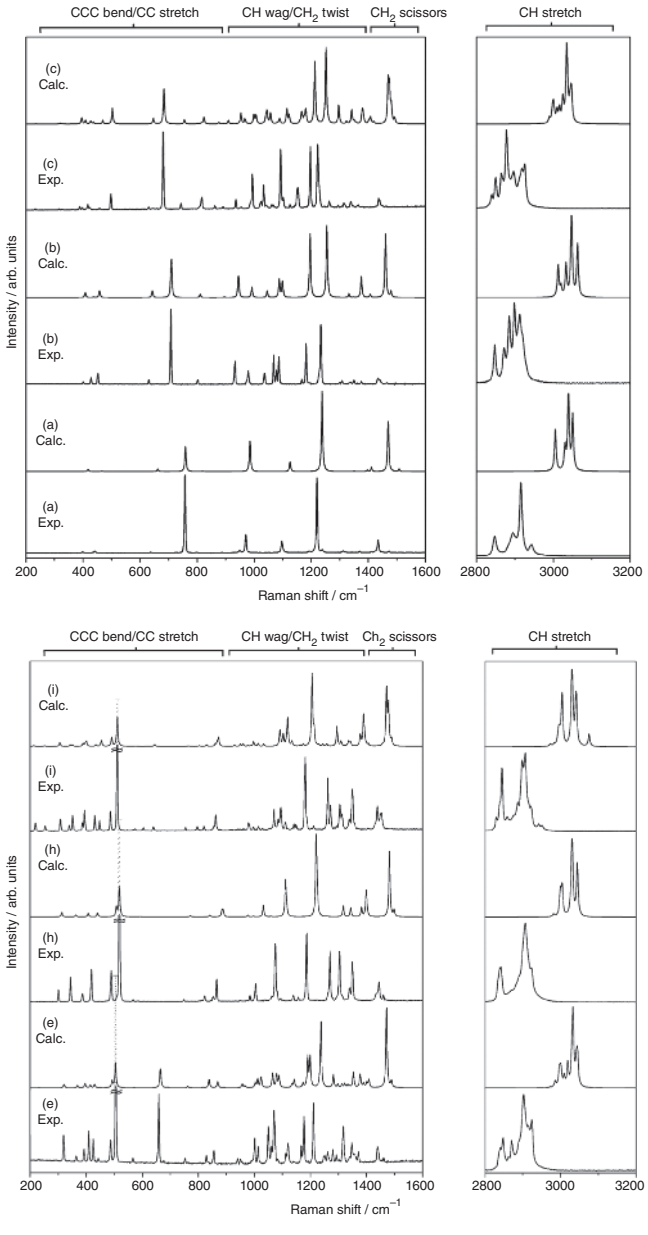

Figure 1.19 *Top*: Experimental and computed Raman spectra (from bottom) for (a) **AD**, (b) **DIA**, (c) and **TRIA**. *Bottom*: Experimental and computed spectra (from bottom) for (e) **1(2)3TRIA**, (h) **1(2,3)4PENT**, and (i) 3-methyl-**1(2,3)4PENT**. Source: Reproduced from Ref. [95] with permission from Elsevier, 2006.

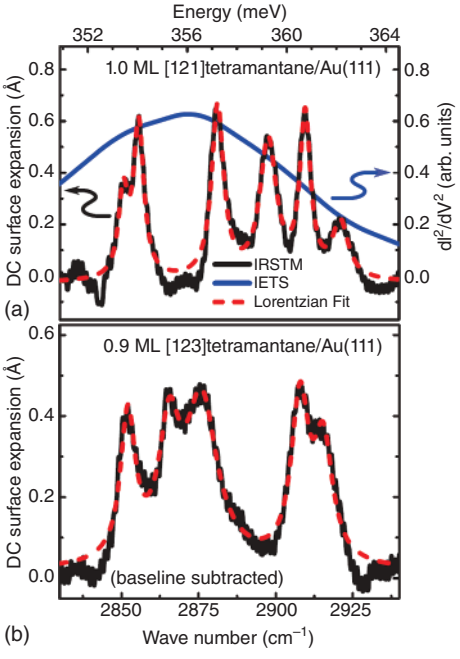

Figure 1.20 Molecular IR absorption of **121TET** (top) and **123TET** (bottom) deposited on Au(111) surface. The blue line shows the unresolved broad peak from STM inelastic electron tunneling spectroscopy (IETS) measurements. Source: Reproduced from Ref. [97] with permission from the American Physical Society, 2013.

group introduction (so-called "doping" that will be discussed in detail in Chapter 12) can be performed using readily available Raman spectroscopy. In a subsequent study, diamondoid dimers and trimers connected with either a single or a double C—C bond and consisting of combinations of **AD** and **DIA** cages were characterized with valence photoelectron spectroscopy [100]. When a double bond is present in the molecule, it significantly impacts the electronic structure of the HOMO, in contrast to molecules with connecting single bonds, where the impact is only small. Moreover, the orbital superposition of both cages in the singly bonded particles determines the overall electronic structure of such systems. This combination of orbitals directly influences the ionization potentials, as homo-dimers have IP values below those of the corresponding monomers, and the measured IPs for hetero-dimers strongly depend on particle composition. Composite diamondoids like **DIA** dimers can also form van der Waals crystals, and it was confirmed that the central double bond predominately influences optical properties both in the gas phase, where single molecules are observed, and in the crystalline solid state [101]. Note that optical band gaps in such systems are significantly lowered (by 0.5–1.0 eV) when compared to their saturated analogues.

As we have seen, diamondoids underwent much turbulence in the course of their history. They evolved from being structural curiosities isolated from oil to inspiring target molecules that challenged the limits of synthetic organic chemistry, to becoming multi-gram resources available from nature and useful for medicine, and finally, to affording modern-day applicability as unique building blocks in nanomaterial design. It is satisfying to see that this fascinating class of compounds went full circle: it was first found in and today is efficiently extracted from oil deposits.

Although our main goal is to demonstrate a wide range of chemical transformations feasible on diamondoids and showcase the fascinating properties of the prepared derivatives and nanostructures, it is still good to pause for a moment and admire the simple beauty of these highly symmetrical jewels of nature.

References

1 Decker, H. (1924). Wege zur Synthese des Diamanten. *Z. Angew. Chem.* 37: 795.
2 Schreiner, P.R., Fokin, A.A., Reisenauer, H.P. et al. (2009). [123]Tetramantane: parent of a new family of sigma-helicenes. *J. Am. Chem. Soc.* 131: 11292–11293.
3 Balaban, A.T. and Schleyer, P.v.R. (1978). Systematic classification and nomenclature of diamond hydrocarbons-I: graph-theoretical enumeration of polymantanes. *Tetrahedron* 34: 3599–3609.
4 (a) Shenderova, O.A., Zhirnov, V.V., and Brenner, D.W. (2002). Carbon nanostructures. *Crit. Rev. Solid State Mater. Sci.* 27: 227–356. (b) Mochalin, V.N., Shenderova, O., Ho, D., and Gogotsi, Y. (2012). The properties and applications of nanodiamonds. *Nat. Nanotechnol.* 7: 11–23.
5 Fokin, A.A., Tkachenko, B.A., Fokina, N.A. et al. (2009). Reactivities of the prism-shaped diamondoids [1(2)3]tetramantane and [12312]hexamantane (Cyclohexamantane). *Chem. Eur. J.* 15: 3851–3862.
6 Eckroth, D.R. (1967). A method for manual generation of correct von Baeyer names of polycyclic hydrocarbons. *J. Org. Chem.* 32: 3362–3365.
7 (a) Balaban, A.T. (2012). Partitioned-formula periodic tables for diamond hydrocarbons (diamondoids). *J. Chem. Inf. Model.* 52: 2856–2863. (b) Balaban, A.T. (2013). Diamond hydrocarbons and related structures. In: *Diamond and Related Nanostructures* (ed. M.V. Diudea and C.L. Nagy), 1–27. Dordrecht: Springer Netherlands. (c) Balaban, A.T. and Rucker, C. (2013). How to specify the structure of substituted blade-like zigzag diamondoids. *Cent. Eur. J. Chem.* 11: 1423–1430.
8 Cupas, C., Schleyer, P.v.R., and Trecker, D.J. (1965). Congressane. *J. Am. Chem. Soc.* 87: 917–918.
9 Balaban, A.T. (2013). Diamond hydrocarbons revisited: partitioned formula tables of diamondoids. *J. Math. Chem.* 51: 1043–1055.
10 Wang, Y.T., Zhao, Y.J., Liao, J.H., and Yang, X.B. (2018). Theoretical investigations on diamondoids (C_nH_m, n=10–41): nomenclature, structural stabilities, and gap distributions. *J. Chem. Phys.* 148: 014306.
11 Willey, T.M., Lee, J.R.I., Brehmer, D. et al. (2021). X-ray spectroscopic identification of strain and structure-based resonances in a series of saturated carbon-cage molecules: Adamantane, twistane, octahedrane, and cubane. *J. Vac. Sci. Technol. A* 39: 053208.
12 Engler, E.M., Andose, J.D., and Schleyer, P.v.R. (1973). Critical evaluation of molecular mechanics. *J. Am. Chem. Soc.* 95: 8005–8025.
13 Schleyer, P.v.R., Williams, J.E., and Blanchard, K.R. (1970). Evaluation of strain in hydrocarbons. The strain in adamantane and its origin. *J. Am. Chem. Soc.* 92: 2377–2386.

14 (a) Pitzer, K.S. (1955). London force contributions to bond energies. *J. Chem. Phys.* 23: 1735–1735. (b) Pitzer, K.S. and Catalano, E. (1956). Electronic correlation in molecules III. The paraffin hydrocarbons. *J. Am. Chem. Soc.* 78: 4844–4846.

15 Wodrich, M.D., Wannere, C.S., Mo, Y. et al. (2007). The concept of protobranching and its many paradigm shifting implications for energy evaluations. *Chem. Eur. J.* 13: 7731–7744.

16 Joyce, J.P., Shores, M.P., and Rappe, A.K. (2020). Protobranching as repulsion-induced attraction: a prototype for geminal stabilization. *Phys. Chem. Chem. Phys.* 22: 16998–17006.

17 Dorofeeva, O.V. and Ryzhova, O.N. (2019). Enthalpies of formation of diamantanes in the gas and crystalline phase: comparison of theory and experiment. *Struct. Chem.* 30: 615–621.

18 Rablen, P.R. (2020). A procedure for computing hydrocarbon strain energies using computational group equivalents, with application to 66 molecules. *Chemistry* 2: 347–360.

19 Wheeler, S.E., Houk, K.N., Schleyer, P.v.R., and Allen, W.D. (2009). A hierarchy of homodesmotic reactions for thermochemistry. *J. Am. Chem. Soc.* 131: 2547–2560.

20 (a) Gronert, S. (2009). The folly of protobranching: turning repulsive interactions into attractive ones and rewriting the strain/stabilization energies of organic chemistry. *Chem. Eur. J.* 15: 5372–5382. (b) Kemnitz, C.R. (2013). Electron delocalization explains much of the branching and protobranching stability. *Chem. Eur. J.* 19: 11093–11095.

21 Fokin, A.A., Tkachenko, B.A., Gunchenko, P.A. et al. (2005). Functionalized nanodiamonds Part I. An experimental assessment of diamantane and computational predictions for higher diamondoids. *Chem. Eur. J.* 11: 7091–7101.

22 Bondi, A. (1964). van der Waals volumes and radii. *J. Phys. Chem.* 68: 441–451.

23 Böttger, O. (1937). Über einige organische Verbindungen "diamantoider" Struktur. *Ber. Dtsch. Chem. Ges.* 70: 314–325.

24 Prelog, V. and Seiwerth, R. (1941). Über die Synthese des Adamantans. *Chem. Ber.* 1644–1648.

25 Meerwein, H., Kiel, F., Klösgen, G., and Schoch, E. (1922). Über bicyclische und polycyclische Verbindungen mit Brückenbindung. Über das Bicyclo-[1,3,3]-nonan und seine Abkömmlinge. *J. Prakt. Chem.* 104: 161–206.

26 Seiwerth, R. (1996). Prelog's Zagreb school of organic chemistry (1935–1945). *Croat. Chem. Acta* 69: 379–397.

27 Meerwein, H. and Schürmann, W. (1913). Über eine Synthese von Abkömmlingen des Bicyclo-[1,3,3]-nonans. *Liebigs Ann.* 398: 196–242.

28 Prelog, V. and Seiwerth, R. (1941). Über eine neue, ergiebigere Darstellung des Adamantans. *Ber. Bunsen. Phys. Chem* 1769–1772.

29 Stetter, H., Bänder, O.E., and Neumann, W. (1956). Über Verbindungen mit Urotropin-Struktur, VIII. Mitteil: Neue Wege der Adamantan-Synthese. *Chem. Ber.* 89: 1922–1926.

30 Schleyer, P.v.R. (1957). A simple preparation of adamantane. *J. Am. Chem. Soc.* 79: 3292.

31 Schleyer, P.v.R., Donaldson, M.M., Nicholas, R.D., and Cupas, C. (1962). Adamantane (tricyclo[3.3.1.$1^{3,7}$]decane). *Org. Synth.* 42: 8.

32 Fort, R.C. and Schleyer, P.v.R. (1964). Adamantane: consequences of the diamondoid structure. *Chem. Rev.* 64: 277–300.

33 Schleyer, P.v.R. and Streitwieser, A. (2015). *From the Ivy League to the Honey Pot, The Foundations of Physical Organic Chemistry: Fifty Years of the James Flack Norris Award*, 169–198. Washington, DC: ACS Symposium Series, American Chemical Society.

34 Karle, I.L. and Karle, J. (1965). Crystal and molecular structure of congressane $C_{14}H_{20}$ by X-ray diffraction. *J. Am. Chem. Soc.* 87: 918–920.

35 Gund, T.M., Williams, V.Z., Osawa, E., and Schleyer, P.v.R. (1970). A convenient, high-yield preparation of diamantane (congressane). *Tetrahedron Lett.* 3877–3880.

36 Gund, T.M., Osawa, E., Williams, V.Z. et al. (1974). Preparation of diamantane. Physical and spectral properties. *J. Org. Chem.* 39: 2979–2987.

37 Gund, T.M., Thielecke, W., and Schleyer, P.v.R. (1973). Diamantane - pentacyclo[7.3.1.1^{4,12}.0^{2,7}.0^{6,11}]tetradecane (butanetetraylnaphthalene, 3,5,1,7-1,2,3,4- decahydro). *Org. Synth.* 53: 30–33.

38 Williams, V.Z., Schleyer, P.v.R., Gleicher, G.J., and Rodewald, L.B. (1966). Triamantane. *J. Am. Chem. Soc.* 88: 3862–3863.

39 Burns, W., McKervey, M.A., and Rooney, J.J. (1975). New synthesis of triamantane involving a novel rearrangement of a polycyclic olefin in the gas phase on platinum. *J. Chem. Soc. Chem. Commun.* 965–966.

40 (a) Hamilton, R., McKervey, M.A., Rooney, J.J. et al. (1976). A short synthesis of triamantane. *J. Chem. Soc. Chem. Commun.* 1027–1028. (b) Hollowood, F.S., McKervey, M.A., Hamilton, R., and Rooney, J.J. (1980). Synthesis of triamantane. *J. Org. Chem.* 45: 4954–4958.

41 Osawa, E., Furusaki, A., Hashiba, N. et al. (1980). Thermodynamic rearrangements of larger polycyclic hydrocarbons derived from the 38.5 and 41.5 °C melting dimers of cyclooctatetraene. Crystal and molecular structures of 5-bromoheptacyclo[8.6.0.0^{2,8}.0^{3,13}.0^{4,11}.0^{5,9}.0^{12,16}]hexadecane (5-bromo-[C_2]-bisethanobisnordiamantane), 6,12-dibromoheptacyclo[7.7.0.0^{2,6}.0^{3,15}.0^{4,12}.0^{5,10}.0^{11,16}]hexadecane, and nonacyclo[11.7.1.1^{2,18}.0^{3,16},0^{4,13}.0^{5,10}.0^{6,14}.0^{7,11}.0^{15,20}]docosane (bastardane). *J. Org. Chem.* 45: 2985–2995.

42 Burns, W., Mitchell, T.R.B., McKervey, M.A. et al. (1976). Synthesis and crystal structure of anti- tetramantane, a large diamondoid fragment. *J. Chem. Soc. Chem. Commun.* 893–895.

43 Roberts, P.J. and Ferguson, G. (1977). *anti*-Tetramantane, a large diamondoid fragment. *Acta Crystallogr. B* 33: 2335–2337.

44 Burns, W., McKervey, M.A., Mitchell, T.R.B., and Rooney, J.J. (1978). A new approach to the construction of diamondoid hydrocarbons. Synthesis of *anti*-tetramantane. *J. Am. Chem. Soc.* 100: 906–911.

45 (a) Schwertfeger, H., Fokin, A.A., and Schreiner, P.R. (2008). Diamonds are a chemist's best friend: Diamondoid chemistry beyond adamantane. *Angew. Chem. Int. Ed.* 47: 1022–1036. (b) McKervey, M.A. (1980). Synthetic approaches to large diamondoid hydrocarbons. *Tetrahedron* 36: 971–992.

46 Hopf, H. (2003). Diamonds from crude oil? *Angew. Chem. Int. Ed.* 42: 2000–2002.

47 Landa, S. and Macháček, V. (1933). Sur l'adamantane, nouvel hydrocarbure extrait du naphte *Collect*. *Czech. Chem. Commun.* 5: 1–5.

48 Dahl, J.E., Moldowan, J.M., Peters, K.E. et al. (1999). Diamondoid hydrocarbons as indicators of natural oil cracking. *Nature* 399: 54–57.

49 Dahl, J.E., Liu, S.G., and Carlson, R.M.K. (2003). Isolation and structure of higher diamondoids, nanometer-sized diamond molecules. *Science* 299: 96–99.

50 Dahl, J.E.P., Moldowan, J.M., Peakman, T.M. et al. (2003). Isolation and structural proof of the large diamond molecule, cyclohexamantane ($C_{26}H_{30}$). *Angew. Chem. Int. Ed.* 42: 2040–2044.

51 Hala, S., Landa, S., and Hanus, V. (1966). Isolation of tetracyclo[6.3.1.$0^{2,6}$.$0^{5,10}$]dodecane and pentacyclo[7.3.1.$1^{4,12}$.$0^{2,7}$.$0^{6,11}$]tetradecane (diamantane) from petroleum. *Angew. Chem. Int. Ed.* 5: 1045–1046.

52 Dahl, J.E.P., Moldowan, J.M., Wei, Z. et al. (2010). Synthesis of higher diamondoids and implications for their formation in petroleum. *Angew. Chem. Int. Ed.* 49: 9881–9885.

53 (a) Stauss, S., Miyazoe, H., Shizuno, T. et al. (2010). Synthesis of the higher-order diamondoid hexamantane using low-temperature plasmas generated in supercritical xenon. *Jpn. J. Appl. Phys.* 49: 070213. (b) Shizuno, T., Miyazoe, H., Saito, K. et al. (2011). Synthesis of diamondoids by supercritical xenon discharge plasma. *Jpn. J. Appl. Phys.* 50: 030207. (c) Oshima, F., Stauss, S., Ishii, C. et al. (2012). Plasma microreactor in supercritical xenon and its application to diamondoid synthesis. *J. Phys. D* 45: 402003. (d) Oshima, F., Stauss, S., Inose, Y., and Terashima, K. (2014). Synthesis and investigation of reaction mechanisms of diamondoids produced using plasmas generated inside microcapillaries in supercritical xenon. *Jpn. J. Appl. Phys.* 53: 010214. (e) Ishii, C., Stauss, S., Kuribara, K. et al. (2015). Atmospheric pressure synthesis of diamondoids by plasmas generated inside a microfluidic reactor. *Diamond Relat. Mater.* 59: 40–46.

54 Nakahara, S., Stauss, S., Kato, T. et al. (2011). Synthesis of higher diamondoids by pulsed laser ablation plasmas in supercritical CO_2. *J. Appl. Phys.* 109: 123304.

55 Stauss, S. and Terashima, K. (2016). *Diamondoids: Synthesis, Properties, and Applications*. Jenny Stanford Publishing p. 242.

56 Bamberg, M., Bursch, M., Hansen, A. et al. (2021). $[Cl@Si_{20}H_{20}]^-$: Parent siladodecahedrane with endohedral chloride ion. *J. Am. Chem. Soc.* 143: 10865–10871.

57 Chan, Y.C., Choy, K.K.H., Chan, A.H.C. et al. (2008). Solubility of diamantane, trimantane, tetramantane, and their derivatives in organic solvents. *J. Chem. Eng. Data* 53: 1767–1771.

58 Iwasa, A., Clay, W.A., Dahl, J.E. et al. (2010). Environmentally friendly refining of diamond-molecules via the growth of large single crystals. *Cryst. Growth Des.* 10: 870–873.

59 Filik, J. (2010). Diamondoid hydrocarbons. In: *Carbon Based Nanomaterials*, vol. 65–66 (ed. N. Ali, A. Ochsner, and W. Ahmed), 1–26.

60 Choi, J.H., Eichele, C., Lin, Y.C. et al. (2008). Determination of effective refractive index of molecular diamondoids by Becke line method. *Scr. Mater.* 58: 413–416.

61 Clay, W.A., Sasagawa, T., Kelly, M. et al. (2008). Diamondoids as low-kappa dielectric materials. *Appl. Phys. Lett.* 93: 172901.

62 Yang, F., Lin, Y., Baldini, M. et al. (2016). Effects of molecular geometry on the properties of compressed diamondoid crystals. *J. Phys. Chem. Lett.* 7: 4641–4647.

63 Yang, F., Lin, Y., Dahl, J.E.P. et al. (2014). High pressure Raman and X-ray diffraction study of [121]tetramantane. *J. Phys. Chem. C* 118: 7683–7689.

64 McIntosh, G.C., Yoon, M., Berber, S., and Tomanek, D. (2004). Diamond fragments as building blocks of functional nanostructures. *Phys. Rev. B* 70: 045401.

65 Fokin, A.A. and Schreiner, P.R. (2009). Band gap tuning in nanodiamonds: first principle computational studies. *Mol. Phys.* 107: 823–830.

66 Raty, J.Y., Galli, G., Bostedt, C. et al. (2003). Quantum confinement and fullerenelike surface reconstructions in nanodiamonds. *Phys. Rev. Lett.* 90: 037401.

67 Drummond, N.D., Williamson, A.J., Needs, R.J., and Galli, G. (2005). Electron emission from diamondoids: a diffusion quantum Monte Carlo study. *Phys. Rev. Lett.* 95: 096801.

68 (a) Patrick, C.E. and Giustino, F. (2013). Quantum nuclear dynamics in the photophysics of diamondoids. *Nat. Commun.* 4: 1–7. (b) Demjan, T., Voros, M., Palummo, M., and Gali, A. (2014). Electronic and optical properties of pure and modified diamondoids studied by many-body perturbation theory and time-dependent density functional theory. *J. Chem. Phys.* 141: 064308.

69 Xiong, T., Wlodarczyk, R., Gallandi, L. et al. (2018). Vibrationally resolved photoelectron spectra of lower diamondoids: a time-dependent approach. *J. Chem. Phys.* 148: 044310.

70 Banerjee, S. and Saalfrank, P. (2014). Vibrationally resolved absorption, emission and resonance Raman spectra of diamondoids: a study based on time-dependent correlation functions. *Phys. Chem. Chem. Phys.* 16: 144–158.

71 Barnard, A.S., Russo, S.P., and Snook, I.K. (2003). Structural relaxation and relative stability of nanodiamond morphologies. *Diamond Relat. Mater.* 12: 1867–1872.

72 Willey, T.M., Bostedt, C., van Buuren, T. et al. (2005). Molecular limits to the quantum confinement model in diamond clusters. *Phys. Rev. Lett.* 95: 113401.

73 Landt, L., Kluender, K., Dahl, J.E. et al. (2009). Optical response of diamond nanocrystals as a function of particle size, shape, and symmetry. *Phys. Rev. Lett.* 103: 047402.

74 (a) Richter, R., Wolter, D., Zimmermann, T. et al. (2014). Size and shape dependent photoluminescence and excited state decay rates of diamondoids. *Phys.*

Chem. Chem. Phys. 16: 3070–3076. (b) Voros, M. and Gali, A. (2009). Optical absorption of diamond nanocrystals from *ab initio* density-functional calculations. *Phys. Rev. B* 80: 161411.

75 Raty, J.Y. and Galli, G. (2005). Optical properties and structure of nanodiamonds. *J. Electroanal. Chem.* 584: 9–12.

76 Landt, L., Kielich, W., Wolter, D. et al. (2009). Intrinsic photoluminescence of adamantane in the ultraviolet spectral region. *Phys. Rev. B* 80: 205323.

77 Voros, M., Demjen, T., Szilvasi, T., and Gali, A. (2012). Tuning the optical gap of nanometer-size diamond cages by sulfurization: a time-dependent density functional study. *Phys. Rev. Lett.* 108: 267401.

78 Richter, R., Rohr, M.I.S., Zimmermann, T. et al. (2015). Laser-induced fluorescence of free diamondoid molecules. *Phys. Chem. Chem. Phys.* 17: 4739–4749.

79 Gali, A., Demjan, T., Voros, M. et al. (2016). Electron-vibration coupling induced renormalization in the photoemission spectrum of diamondoids. *Nat. Commun.* 7: 11327.

80 (a) Bilalbegović, G., Maksimović, A., and Valencic, L.A. (2018). Tetrahedral hydrocarbon nanoparticles in space: X-ray spectra. *Mon. Not. R. Astron. Soc.* 476: 5358–5364. (b) Bauschlicher, C.W., Liu, Y.F., Ricca, A. et al. (2007). Electronic and vibrational spectroscopy of diamondoids and the interstellar infrared bands between 3.35 and 3.55 μm. *Astrophys. J.* 671: 458–469. (c) Pirali, O., Vervloet, M., Dahl, J.E. et al. (2007). Infrared spectroscopy of diamondoid molecules: new insights into the presence of nanodiamonds in the interstellar medium. *Astrophys. J.* 661: 919–925. (d) Bouwman, J., Horst, S., and Oomens, J. (2018). Spectroscopic characterization of the product ions formed by electron ionization of adamantane. *ChemPhysChem* 19: 3211–3218. (e) Greaves, J.S., Scaife, A.M.M., Frayer, D.T. et al. (2018). Anomalous microwave emission from spinning nanodiamonds around stars. *Nat. Astron.* 2: 662–667.

81 Steglich, M., Huisken, F., Dahl, J.E. et al. (2011). Electronic spectroscopy of FUV-irradiated diamondoids: a combined experimental and theoretical study. *Astrophys. J.* 729: 91.

82 Mutschke, H., Andersen, A.C., Jager, C. et al. (2004). Optical data of meteoritic nano-diamonds from far-ultraviolet to far-infrared wavelengths. *Astron. Astrophys.* 423: 983–993.

83 (a) Lu, A.J., Pan, B.C., and Han, J.G. (2005). Electronic and vibrational properties of diamondlike hydrocarbons. *Phys. Rev. B* 72: 035447. (b) Lenzke, K., Landt, L., Hoener, M. et al. (2007). Experimental determination of the ionization potentials of the first five members of the nanodiamond series. *J. Chem. Phys.* 127: 084320.

84 National Institute of Standard, *NIST Chemistry webbook*. http://webbook.nist.gov/chemistry.

85 Meunier, M., Quirke, N., and Binesti, D. (1999). The calculation of the electron affinity of atoms and molecules. *Mol. Simul.* 23: 109–125.

86 de Urquijo, J., Arriaga, C.A., Cisneros, C., and Alvarez, I. (1999). A time-resolved study of ionization, electron attachment and positive-ion drift in methane. *J. Phys. D* 32: 41–45.

87 Bowers, K.W., Greene, F.D., and Nolfi, G.J. (1963). Radical anions of adamantane and hexamethylenetetramine. *J. Am. Chem. Soc.* 85: 3707.

88 Jones, M.T. (1966). The reported adamantane anion radical. Its relationship to benzene anion radical. *J. Am. Chem. Soc.* 88: 174–176.

89 Li, Q.S., Feng, X.J., Xie, Y., and Schaefer, H.F. (2005). Perfluoroadamantane and its negative ion. *J. Phys. Chem. A* 109: 1454–1457.

90 Irikura, K.K. (2008). Sigma stellation: a design strategy for electron boxes. *J. Phys. Chem. A* 112: 983–988.

91 Li, J.R., Niesner, D., and Fauster, T. (2021). Negative electron affinity of adamantane on Cu(111). *J. Phys. Condens. Matter* 33: 135001.

92 Wang, Y., Kioupakis, E., Lu, X. et al. (2008). Spatially resolved electronic and vibronic properties of single diamondoid molecules. *Nat. Mater.* 7: 38–42.

93 Oomens, J., Polfer, N., Pirali, O. et al. (2006). Infrared spectroscopic investigation of higher diamondoids. *J. Mol. Spectrosc.* 238: 158–167.

94 Richardson, S.L., Baruah, T., Mehl, M.J., and Pederson, M.R. (2006). Cyclohexamantane ($C_{26}H_{30}$): first-principles DFT study of a novel diamondoid molecule. *Diamond Relat. Mater.* 15: 707–710.

95 Filik, J., Harvey, J.N., Allan, N.L. et al. (2006). Raman spectroscopy of diamondoids. *Spectrochim. Acta A Mol. Biomol. Spectrosc.* 64: 681–692.

96 Richardson, S.L., Baruah, T., Mehl, M.J., and Pederson, M.R. (2005). Theoretical confirmation of the experimental Raman spectra of the lower-order diamondoid molecule: cyclohexamantane ($C_{26}H_{30}$). *Chem. Phys. Lett.* 403: 83–88.

97 Pechenezhskiy, I.V., Hong, X., Nguyen, G.D. et al. (2013). Infrared spectroscopy of molecular submonolayers on surfaces by infrared scanning tunneling microscopy: Tetramantane on Au(111). *Phys. Rev. Lett.* 111: 126101.

98 Zhuang, C.Q., Jiang, X., Zhao, J.J.J. et al. (2009). Infrared spectra of hydrogenated nanodiamonds by first-principles simulations. *Phys. E: Low-Dimens. Syst. Nanostructures* 41: 1427–1432.

99 Meinke, R., Richter, R., Merli, A. et al. (2014). UV resonance Raman analysis of trishomocubane and diamondoid dimers. *J. Chem. Phys.* 140: 034309.

100 Zimmermann, T., Richter, R., Knecht, A. et al. (2013). Exploring covalently bonded diamondoid particles with valence photoelectron spectroscopy. *J. Chem. Phys.* 139: 084310.

101 Tyborski, C., Meinke, R., Gillen, R. et al. (2017). From isolated diamondoids to a van-der-Waals crystal: a theoretical and experimental analysis of a trishomocubane and a diamantane dimer in the gas and solid phase. *J. Chem. Phys.* 147: 044303.